Journal of Biomedical Optics

BiomedicalOptics.SPIEDigitalLibrary.org

Hybrid imaging of fluorescently labeled cancer drugs and label-free four-wave mixing microscopy of cancer cells and tissues

Rick Krabbendam
Martin Pool
Liesbeth G. de Vries
Herman L. Offerhaus
Jennifer L. Herek
Cees Otto

SPIE.

Hybrid imaging of fluorescently labeled cancer drugs and label-free four-wave mixing microscopy of cancer cells and tissues

Rick Krabbendam,[a,*] Martin Pool,[b] Liesbeth G. de Vries,[b] Herman L. Offerhaus,[a] Jennifer L. Herek,[a] and Cees Otto[c,*]
[a]University of Twente, Optical Sciences Group, MESA+ Institute for Nanotechnology, Drienerlolaan 5, Enschede 7500AE, The Netherlands
[b]University Medical Centre Groningen, Department of Medical Oncology, DA13, Hanzeplein 1, 9713 GZ, Groningen, The Netherlands
[c]University of Twente, MIRA Institute for Biomedical Technology and Technical Medicine, Medical Cell BioPhysics Group, Drienerlolaan 5, Enschede 7500AE, The Netherlands

Abstract. Fluorescent labels are well suited as tracers for cancer drug monitoring. Identifying cellular target regions of these drugs with a high resolution is important to assess the working principle of a drug. We investigate the applications of label-free nonresonant four-wave mixing (NR-FWM) microscopy in biological imaging in combination with fluorescence imaging of fluorescently labeled cancer drugs. Results from human A431 tumor cells with stained nuclei and incubated with IRdye 800CW labeled cancer drug cetuximab targeting epidermal growth factor receptor at the cell membrane show that NR-FWM is well suited for cellular imaging. A comparison of vibrationally nonresonant FWM imaging with vibrational resonant coherent anti-Stokes Raman scattering signals revealed nearly identical qualitative information in cellular imaging. NR-FWM is also suitable for tumor tissue imaging in combination with fluorescence imaging of IRdye 800CW labeled, human epidermal growth factor 2 targeting cancer drug pertuzumab and provides additional information over transmission microscopy. [DOI: 10.1117/1.JBO.20.8.086006]

Keywords: nonlinear microscopy; multimodal microscopy; cancer drugs; fluorescence imaging.

Paper 140659RRR received Oct. 8, 2014; accepted for publication Jul. 21, 2015; published online Aug. 13, 2015.

1 Introduction

An important step in the development and testing of new targeted cancer drug candidates is the acquisition of information about their pharmacological and pharmacodynamic action. Targeted cancer drugs are designed to bind to specific biomolecules, involved in carcinogenesis and tumor growth, such as membrane proteins or ligands, for their effectiveness. To assess their effectiveness, the identification of target regions within a tumor with a high, subcellular resolution is a key aspect.

Monoclonal antibodies (mAbs), such as cetuximab and trastuzumab, are currently used as targeted cancer drugs.[1] Cetuximab and trastuzumab are targeted to, respectively, the extracellular domain of human epidermal growth factor receptor (EGFR) and the human epidermal growth factor 2 (HER2) receptor at the cell membrane. Both EGFR and HER2 are implicated in regulating cell growth and proliferation and are frequently overexpressed, mutated, or dysregulated in certain cancer types. mAbs with their high affinity are suitable candidates for treatment, or when radioactively or fluorescently labeled, as tracer for tumors expressing these targets.[2–4]

One of the strategies to use an mAb as an imaging tracer for tumors is the labeling of the antibody with a fluorescent dye. Studies involving the above-mentioned mAbs use IRdye 800CW for antibody labeling.[4] The use of a dye with absorption and emission spectra in the 800 nm wavelength region circumvents the influence of autofluorescent molecules, such as reduced nicotinamide adenine dinucleotide and flavin adenine dinucleotide and other native proteins, since these emit no red-shifted autofluorescence in this wavelength region.[5] Also, because IRdye 800CW absorbs and emits in the optical window of tissue, the loss of excitation light and fluorescence emission due to absorption and scattering by tissue is minimal.[6] IRDye 800CW has been tested for toxicity and approved by the FDA for human use.[7] This combination of properties makes this particular dye optimal for fluorescence imaging *in vivo*.[8]

Detection of drugs has been investigated extensively both *in vivo* and in model systems to assess the distribution of the drug in both healthy organs and malignant tumor tissue and to localize the binding targets of the cancer drugs. Currently, the microscopic localization and distribution of cancer drugs is most commonly investigated using immunohistochemistry in combination with hematoxylin and eosin staining.[4,9,10] Simultaneously, information about the location of the different cellular components is obtained mostly using fluorescent probes targeted to specific cellular components.[11] Immunohistochemistry has a limited resolution, and the addition of stains to visualize, for example, nuclei or blood vessels enables only selective imaging of the targets of the stains but does not provide information about other structures. The effects of adding stains to a biological system are not always known and could influence the biological process under investigation. Although the location of other cell components can be determined with a high three-dimensional (3-D) resolution using multiphoton

*Address all correspondence to: Rick Krabbendam, E-mail: r.krabbendam@utwente.nl; Cees Otto, E-mail: c.otto@utwente.nl

1083-3668/2015/$25.00 © 2015 SPIE

excitation of stains,[12] this technique is still limited in the sense that it is only sensitive to cellular structures that can be stained. Conventional (linear) microscopy techniques, such as bright-field and phase contrast microscopy, are able to provide morphological information about the sample, but only with a low resolution in 3-D. In contrast, nonlinear optical imaging techniques, such as coherent anti-Stokes Raman scattering (CARS), provide a label-free, inherently confocal method to image cellular morphology with a high resolution.

CARS microscopy is a nonlinear optical technique that is widely applied in biological imaging of cells and tissue,[13] imaging of pharmaceutical compounds,[14] and imaging of drug distribution in cells and tissue.[15,16] While most microscopy techniques require the addition of contrast agents, such as fluorophores, CARS microscopy techniques are label-free since they exploit differences in vibrational energy levels between different chemicals. When the energy difference between the two input beams, pump (ω_p) and Stokes (ω_s), is equal to the energy of a molecular vibration, an additional amplitude in the anti-Stokes field is generated at frequency $\omega_{as} = 2\omega_p - \omega_s$. Due to the quadratic dependence of the CARS signal on the incident pump laser power, the anti-Stokes field is generated mostly in focus. CARS microscopy, thus, enables mapping of molecular information with a high resolution in x, y, and z. A common contribution to the total anti-Stokes signal in CARS imaging, however, is the presence of a nonresonant four-wave mixing (NR-FWM) signal, also referred to as the nonresonant background.[17] This contribution is dependent on the electronic polarizability only. We will show that the vibrationally nonresonant FWM process is useful for morphological imaging and can be combined with molecule-specific linear fluorescence imaging of IRdye 800CW labeled mAbs cetuximab and pertuzumab. Cetuximab and pertuzumab are used to target EGFR and HER2, respectively. We also combine NR-FWM microscopy with two-photon excitation fluorescence (TPEF) imaging of Hoechst 33342 or 4',6-diamidino-2-phenylindole (DAPI) stained nuclei, respectively. For this, both cell and xenograft tumor tissue samples are used. Figure 1 shows an energy level diagram of the mentioned optical processes. Morphological NR-FWM imaging here is based on spatial variations in the molecular and electronic density in the sample and, therefore, spatial variations of the amplitude of the generated anti-Stokes signal. The generated NR-FWM intensity is compared with vibrational resonant CARS signals in order to extract insights on the advantages and drawbacks of the CARS and NR-FWM imaging modalities.

2 Theoretical Background

This section describes the theoretical background of CARS, NR-FWM, and the relation between the total anti-Stokes signal and the third-order nonlinear susceptibility χ^3.

The total anti-Stokes signal (I_{AS}) is related to the third-order susceptibility (χ^3). The susceptibility χ^3 is generally described by a vibrationally resonant (χ^3_R) and a vibrationally nonresonant or electronic part (χ^3_{NR}).[17]

$$I_{AS} \propto |\chi^3_R + \chi^3_{NR}|^2 = |\chi^3_R|^2 + 2\chi^3_{NR}\mathrm{Re}[\chi^3_R] + |\chi^3_{NR}|^2. \quad (1)$$

Here the resonant part describes the interaction of the pump and Stokes field with a molecule through a coupling with two vibrational energy levels in the electronic ground state of a molecule, whereas the nonresonant contribution describes interactions of the pump and Stokes field with a molecule through a (often nonresonant) coupling to excited electronic

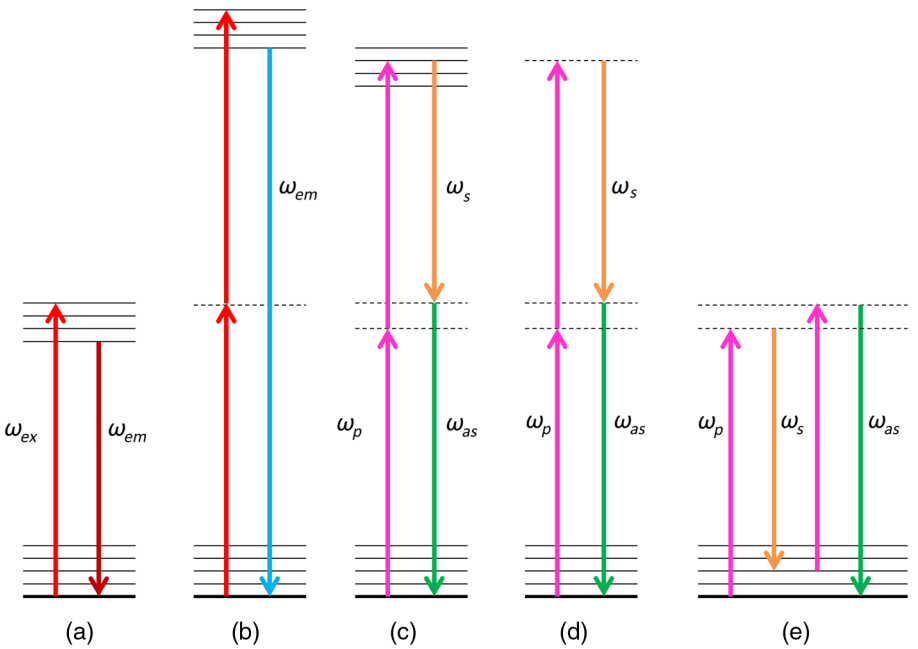

Fig. 1 (a) Energy level diagram of linear fluorescence, (b) two-photon excited fluorescence, (c) electronic resonant (NR) four-wave mixing (FWM), (d) electronic nonresonant FWM, and (e) vibrational resonant FWM [or coherent anti-Stokes Raman scattering (CARS)]. The frequency used for one- and two-photon excitation is ω_{ex} (in red), with corresponding emission frequency ω_{em} [dark red and blue in the linear and two-photon excitation fluorescence (TPEF) energy level diagram, respectively]. ω_p (in purple) and ω_s (in orange) are the applied pump and Stokes fields in nonresonant FWM or a CARS experiment, and ω_{as} (in green) indicates the generated anti-Stokes field.

states to generate an anti-Stokes photon. In the latter process, no vibrational energy level is probed. An anti-Stokes signal is also generated when the difference frequency between the pump and probe beams is far from any vibrational resonance in the electronic ground state. This off-resonance contribution also contributes nonresonant signal to I_{AS} [Eq. (1)]. The spectrum of the interferometric mixing term $2\chi^3_{NR}\mathrm{Re}[\chi^3_R]$ in Eq. (1) rapidly changes when $\omega_p - \omega_s \approx \omega_{\mathrm{vib}}$, i.e., in the neighborhood of a vibrational resonance. This spectral response arises from the rapidly changing vibrational phase that is associated with the vibrational resonant transition, with respect to the phase of χ^3_{NR}. Although the processes described by χ^3_{NR} are usually assumed to have a flat phase, resulting in a purely real χ^3_{NR}, electronically resonant FWM may also contribute a phase change to the anti-Stokes signal. Far away from excited state electronic resonances, this phase change is mostly small and contributes a constant phase, a flat phase, to the total phase in a CARS spectrum.

The total generated anti-Stokes intensity depends not only on the material property χ^3 but also on the cubic product of intensities of the pump and Stokes beams.[18]

$$I_{AS} \propto I^2_{\mathrm{pump}} I_{\mathrm{Stokes}}. \tag{2}$$

The aim of CARS experiments is commonly to acquire material-specific information by probing vibrational resonances. The signal-to-noise ratio (SNR) of this signal is reduced due to the nonresonant contributions to I_{AS}. Therefore, reduction of the NR-FWM signals while generating vibrational resonant signals is a major goal in CARS research. Methods implemented in CARS microscopy to reduce the nonresonant background are based on well-known techniques in CARS spectroscopy and include polarization CARS,[19,20] frequency modulated CARS,[21] or heterodyne CARS.[17] These techniques improve the SNR of the CARS signal. Although the removal of the NR-FWM signals increases the chemical specificity of resonant CARS techniques, the vibrationally nonresonant FWM signals could be used to generate contrast in samples. Because the vibrationally nonresonant FWM signal contributions are generated by all sample components, unlike the resonant contributions, these nonresonant contributions can be used to image cellular and tissue structures.

Some work on NR-FWM imaging of biological samples has been performed. Mahou et al.[22] applied NR-FWM microscopy to image *C. Elegans worms* and zebra fish embryos and showed that spatial variations in χ^3_{NR} can be used to image cells and cell substructures. Comparisons among NR-FWM microscopy, third harmonic generation (THG), second harmonic generation (SHG), and TPEF by Mahou et al.[22] showed that each of these techniques has a specific advantage: NR-FWM microscopy provides label-free contrast in the sample based on spatial variations in χ^3. THG enables label-free imaging of interfaces in the sample due to large differences in χ^3 at interfaces, but requires higher power than NR-FWM for a 250 fs pulse duration. SHG and TPEF can be used for (label-free) molecule-specific imaging.

Min et al.[23] applied NR-FWM microscopy with a small difference in wavelength between pump and Stokes beams (near-degenerate NR-FWM) to image live A549 human nonsmall cell lung cancer cells and muscle and brain tissue morphology. Min et al.[23] used near-degenerate electronic resonant FWM microscopy to image absorbing but nonfluorescent molecules by tuning the pump wavelength to match the absorption band of the molecule. Potma et al.[17] showed that the nonresonant FWM intensity produced at different locations in a single NIH-3T3 mouse fibroblast cell can be used to generate contrast in the cell. The recorded NR-FWM image of a single NIH-3T3 cell shows the cell membrane and the nucleus and the overall morphology.

3 Materials and Methods

3.1 *Sample Preparation*

Cetuximab (Erbitux®, Merck KgaA) and pertuzumab (Perjeta®, Roche) are buffer exchanged into 0.9% NaCl using Vivaspin 2 ultracentrifuge concentrators (GE Healthcare). After pH is set to 9.0 with 0.2 M sodium carbonate, IRDye 800CW-NHS ester in dimethyl sulfoxide (DMSO) at 5 mg/mL (Licor Biosciences) is added in a 1:3 (cetuximab) and 1:2 (pertuzumab) molar ratio of antibody to IRDye 800CW-NHS and incubated during 1 h at 20°C. Purification of antibody-dye conjugates from unreacted dye is performed using PD10 desalting columns (GE Healthcare). Final concentration, purity, and labeling efficacy are analyzed using size-exclusion, high-performance liquid chromatography with absorbance detection wavelengths at 220, 280, and 780 nm. Cetuximab-IRDye 800CW yielded 2.6 dye-molecules/mAb, whereas pertuzumab-IRDye 800CW yielded 1.7 dye-molecules/mAb; both products were over 95% pure. Cetuximab-IRdye 800CW is used for single cell imaging, and pertuzumab-IRdye 800CW is used for the breast cancer model (vide infra). Because the mass ratio between a single antibody and a single IRdye 800CW molecule is between 150 kDa to 1 kDa and 170 kDa to 1 kDa, the obtained labeling ratio for cetuximab and pertuzumab antibodies has only a small effect on the total weight of the original antibody. Also, as the antigen binding site of the antibodies is very small compared to the total antibody, it is unlikely that the antigen binding site is occupied by one or more IRdye 800CW molecules at the mentioned labeling ratios.

Cellular imaging is performed using the EGFR-overexpressing human squamous cell carcinoma cell line A431. A431 cells are cultured in Dulbecco's modified Eagles medium with high glucose supplemented with 10% fetal bovine serum. Cetuximab-IRdye 800CW is added to the cells at a concentration of 20 μg/mL, which amounts to 10 μg for a 2 cm^2 monolayer of cells. This results in 4.1×10^{13} antibody molecules per 120,000 cells. The incubation time is 30 min at 37°C. The cells are fixed in a 4% paraformaldehyde solution in phosphate-buffered saline (PBS) for 15 min. Nuclei are stained by a 0.1 μg/mL Hoechst H33342 solution during 20 min incubation.

All animal experiments are approved by the Institutional Animal Care and Use Committee of the University of Groningen. For tissue imaging, male Balb/C nude mice (BALB/cOlaHsd-Foxn1nu, Harlan) are used. Xenografts are inoculated subcutaneously using HER2 overexpressing SK-BR-3 breast cancer in a 1:1 mixture of PBS and matrigel. When tumors measured 100 to 200 mm^3, mice are injected with 100 μg pertuzumab-IRdye 800CW via the penile vein and sacrificed six days postinjection. Xenografts are excised and fixed in 4% neutral buffered formaldehyde solution, paraffin embedded, and slices with a thickness of 4 μm are cut. Slices are placed on a cover glass using a warm water bath and dried overnight at 60°C. Subsequently, slices are de-paraffinized and the nuclei stained with DAPI.

3.2 *Optical Microscopy*

Linear fluorescence, nonlinear fluorescence, and CARS microscopy are performed on an Olympus IX71 inverted microscope, equipped with a FluoView300 scan unit. A set of galvo mirrors scans the beams over the sample to generate a two-dimensional image.

The excitation light is produced by an optical parametric oscillator (OPO, APE Berlin GmbH, Germany) pumped by a 22 ps pulsed, frequency-doubled Nd:YVO_4 1064 nm wavelength laser (Coherent Paladin). The narrowband signal output of the OPO is tunable from 710 to 980 nm by changing the crystal temperature and a Lyot filter installed in the OPO cavity.[24] The idler output of the OPO is not used.

A part of the laser fundamental at 1064 nm beam is directed to the microscope. Before it enters the microscope, it is spatially overlapped with the OPO signal beam using a dichroic mirror and temporally overlapped using a delay stage in the 1064 nm beam path. The signal beam and fundamental beam are used as pump and Stokes beam, respectively, for the generation of CARS and NR-FWM signals. For vibrationally resonant CARS images, the frequency difference between the signal and 1064 nm beam is set to match the CH_2-stretch vibrations at 2845 cm^{-1}. For NR-FWM imaging, the frequency difference is set to 2698 cm^{-1}, within the silent region for Raman spectroscopy.[25] At this frequency, the anti-Stokes signal contains no vibrational resonant contributions from biomolecules. The wavelength of the anti-Stokes signal was 676 nm for a difference of 2698 cm^{-1} between the pump and Stokes beam. The frequency of 2698 cm^{-1} was selected to optimize for the wavelength-dependent transmission efficiency of the setup in combination with the available optical filters as well as the wavelength-dependent detection efficiency of the photodetector. For SHG, only the 1064 nm beam is used.

For clarification, an overview of the different modalities with corresponding excitation wavelengths is shown in Fig. 2. Figure 2 also shows a measured averaged background-free spontaneous Stokes Raman spectrum of an A431 cell. The spontaneous Raman spectrum was measured on a different microscope described elsewhere,[26] using a 647.1 nm continuous wave laser and a home-built spectrometer. This spectrum was measured at the Stokes side, but plotted at the anti-Stokes side of the pump beam (indicated by the magenta arrow labeled ω_p) used in the CARS modality at 2845 cm^{-1}. In this figure, the spectral locations of the imaging modalities NR-FWM, CARS, TPEF, and linear fluorescence explained in Fig. 1 are shown using corresponding color-coding. The IRdye 800CW excitation beam is shown in red at 770 nm (ω_{ex}), with corresponding emission at 800 nm in dark red (ω_{em}). The two-photon excitation modality used to excite Hoechst 33342 and DAPI is indicated by the two red arrows at 385 nm wavelength, representing the two 770 nm photons involved. The corresponding Hoechst 33342 emission is represented by the blue arrow at 400 nm (ω_{em}). From the spontaneous Raman spectrum, it can be seen that CARS at 2845 cm^{-1} (green solid, ω_{as}) is measured at resonance in the CH-stretch region and that the NR-FWM at 2698 cm^{-1} (green dashed, ω_{as}) is measured off-resonance. Note that the 2845 cm^{-1} peak is relatively small compared to the total intensity in the CH-stretch region. This could be different in CARS experiments, since the signals in CARS experiments are generated coherently. The NR-FWM anti-Stokes signal at 2698 cm^{-1} is represented by a dashed line. In our experiments, the wavelength of the pump beam is tuned,

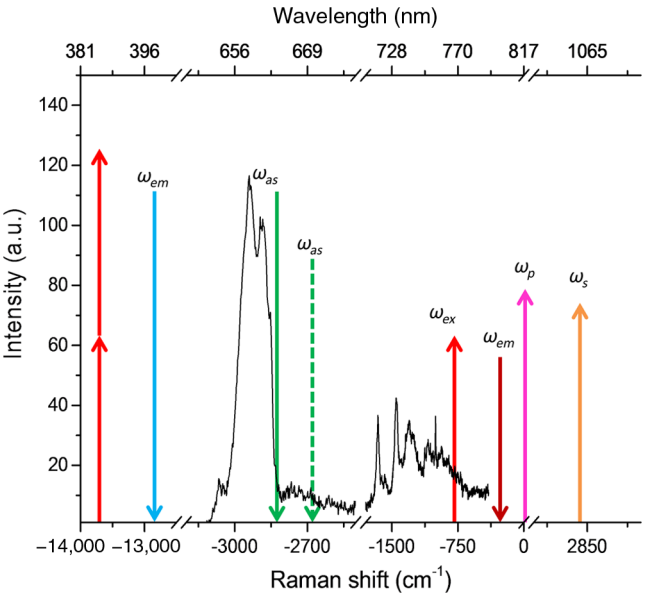

Fig. 2 Spontaneous Stokes Raman spectrum plotted at the anti-Stokes side of the pump beam at 0 cm^{-1}. The Raman spectrum is divided in the CH-stretch region (−3200 to −2500 cm^{-1}) and the fingerprint region (−1800 to 0 cm^{-1}). The imaging modalities are also indicated in this figure at the corresponding wavelength with respect to the Raman spectrum. The location of the different excitation beams and the detected signals as shown in Fig. 1 are overlaid on the Raman spectrum. The detected signals are the vibrationally nonresonant FWM signal at 2698 cm^{-1} (dashed green, ω_{as}), vibrationally resonant CARS (solid green, ω_{as}), Hoechst TPEF emission (blue, ω_{em}), and IRdye 800CW fluorescence emission (dark red, ω_{em}).

such that only the wavenumber axis represents the NR-FWM modality correctly. The Stokes beam, at 1064 nm, is shown at the Stokes side of the pump beam in orange (ω_s). For excitation of the IRdye 800CW fluorophore, the signal beam is tuned to 770 nm. A power of 40 μW was used. For TPEF of Hoechst 33342 and DAPI, the power of the signal beam at 770 nm was increased to 50 mW. Resonant CARS and FWM images were recorded at excitation powers of 50 and 95 mW for the signal beam and 1064 nm for Stokes beam, respectively.

Both beams are focused on the sample using a 60 × 1.2 NA Olympus water immersion objective (UPLANSAPO IR, Olympus). IRdye 800CW, Hoechst 33342, and DAPI fluorescence are collected using the 1.2 NA objective and detected with a photomultiplier tube (PMT, Hamamatsu, R3896) in backward detection mode. Vibrationally resonant CARS and the NR-FWM signals are detected in the forward direction using a 0.55 NA condenser. Appropriate filters were placed in front of the PMT (Hamamatsu, R3896) to reject the pump and Stokes beams. Images are recorded with a pixel dwell time of 10 microseconds and typically three averages. Nyquist sampling criteria are satisfied for the one-photon and multiphoton imaging modalities. Transmission images were recorded by detecting the transmitted intensity of the pump beam at 770 nm while the beam scans over the cell, using a fiber coupled to a PMT. All images were corrected for the spatial variations in collection efficiency of the generated signals. This was done by measuring the CARS signal of a droplet of DMSO, which is expected to generate a homogeneous CARS intensity in the field of view. Any nonhomogeneous intensities in the image

correspond to spatial variations in collection efficiencies. This signal has been used for correction of the images.

4 Results and Discussion

4.1 *Cellular Imaging*

In Fig. 3(c), a laser light transmission image of a single, DAPI-stained, A431 cell incubated with cetuximab-IRdye 800CW is shown. Figure 3(a) shows the corresponding fluorescence emission image of cetuximab-IRdye 800CW. Figure 3(b) shows a TPEF image of Hoechst 33342, indicating the location of the cell nucleus with an inherently confocal resolution. The image size is 78×78 μm consisting of 1024×1024 pixels. All images are recorded at the same z-position of the objective and the same field of view.

The transmission and Hoechst 33342 images provide information about cellular morphology, whereas the fluorescence image provides information about the location of the cancer drug cetuximab with high selectivity. The combination of images suggests that the fluorescently labeled cetuximab is present mainly at the cell membrane, as expected; the shape of the fluorescence emission completely surrounds the nucleus in the two-dimensional image plane. Some fluorescence intensity can be seen from the distal ends of the cell or from intracellular regions. By comparing the fluorescence emission image [Fig. 3(a)] with the transmission image [Fig. 3(c)], the fluorescence emission appears to colocalize with the cell membrane. Because the signals recorded in the transmission and linear fluorescence image also contain contributions from out-of-focus regions in the cell, it is difficult to determine the exact location of the fluorescence emission image with respect to the cell membrane and other cellular components. Both discussed methods, Hoechst staining and transmission microscopy, have their limitations in the sense that only information about the location of a certain cellular compound (nucleus stained with Hoechst 33342) is obtained or that the depth resolution is relatively low (transmission image).

In Fig. 3, the one- and two-photon fluorescence modalities are combined with the nonlinear label-free optical imaging modalities CARS and NR-FWM microscopy in Figs. 3(d) and 3(e), respectively. Figure 3(d) shows a CARS image at 2845 cm^{-1}, probing the CH_2 stretching vibrations, predominantly present in lipids.[27] This image shows the vibrationally resonant anti-Stokes signals arising from lipid structures in the A431 cells on top of the vibrationally nonresonant FWM signals that are also present at this vibrational frequency. An image of the same cell far from vibrational resonances was recorded at 2698 cm^{-1} [Fig. 3(e)], to qualitatively compare the differences and similarities between the image at resonance 2845 cm^{-1} [Fig. 3(d)] and an off-resonance image. It can be observed from a comparison between Figs. 3(d) and 3(e) that the vibrationally nonresonant FWM contribution dominates the response in the image recorded at resonance. A large part of the signal could also arise from the interferometric mixing term as stated in Eq. (1). The interferometric mixing term dominates over the purely vibrational resonant term when the

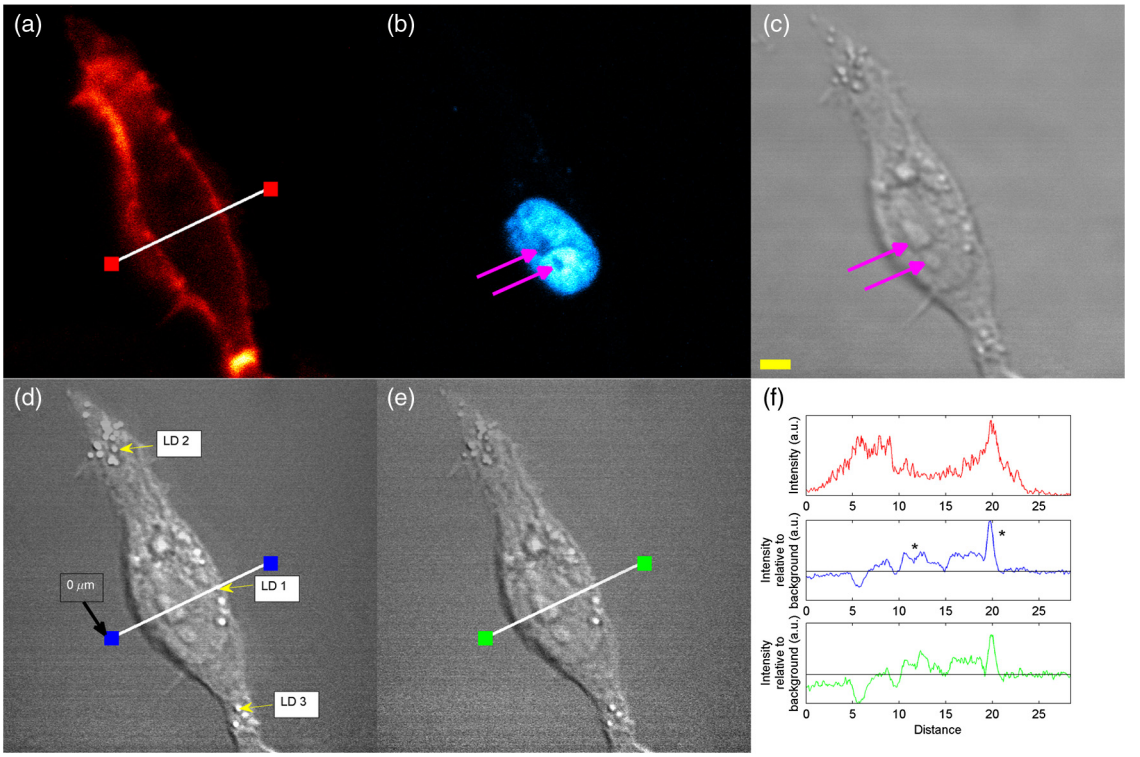

Fig. 3 Multimodal images of fixed A431 cells, incubated with cetuximab-IRdye 800CW and stained with Hoechst 33342. The images show (a) the IRdye 800CW fluorescence emission image, (b) Hoechst 33342 TPEF image, (c) laser transmission image, (d) CARS image at 2845 cm^{-1}, and (e) NR-FWM image at 2698 cm^{-1}. The size of the scale bar shown in (c) is 5 μm [relevant for panels (a) to (e)]. The intensity profile plot of the white line in (a), (d), and (e) is shown in (f). The black line shows the average background intensity. The arrows in (d) indicate the lipid droplets (LDs) that were used for quantitative analysis in Table 1.

nonresonant contributions are large compared to the vibrational resonant contributions.

The image in Fig. 3(d) shows the morphology of the cell. The cell membrane, cell nucleus, and two nucleoli can be identified. The nucleoli are specialized areas in the nucleus, which correlate with the dark spots in the Hoechst TPEF emission image in Fig. 3(b), as indicated by the purple arrows. Lipid droplets produce a large anti-Stokes intensity at 2845 cm^{-1}. A large amount of lipid droplets is located in the upper left corner of the cell in Fig. 3(d). Also, in other regions of the cell, lipid-rich structures can be identified. The lipid droplets, nucleoli, and the nucleus can also be identified in the NR-FWM image in Fig. 3(e).

Intensity profiles are shown in Fig. 3(f). The profiles show the intensity of the IRdye 800CW fluorescence emission, the CARS, and the NR-FWM signals as measured along the white line in Figs. 3(a), 3(d), and 3(e). The colors of the curves in Fig. 3(f) correspond with the lines in the figures marked with identical colors. These profiles are shown to compare the signal measured in the off-resonance image with the signal measured in the image on resonance. In both the CARS and NR-FWM intensity line profiles, large variations in intensity are observed as a function of position in the cell. This can be compared with a region outside the cell, where a homogeneous body of PBS generates a uniform anti-Stokes signal. From this, it can be concluded that water inside the cell has a significant contribution to the total anti-Stokes signal. Other molecules, such as organic molecules inside the cell soma, could also contribute to the total CARS signal.

In Fig. 3(f), two features, a nucleolus and a lipid droplet, are indicated with a star at 11 and 20 μm, respectively, in the 2845 cm^{-1} intensity profile plot. In the 2845 cm^{-1} profile, the lipid droplet signal is higher compared to the (nonresonant) signal generated by water in the 2698 cm^{-1} profile plot. This indicates the presence of additional mixing term or vibrationally resonant contributions to the total lipid droplet signal at 2845 cm^{-1}.

Although the NR-FWM image at 2698 cm^{-1} is far from any vibrational resonance (Fig. 2), a high contrast can be observed [Fig. 3(e)]. The contrast in the NR-FWM image arises from a combination of molecular density differences and third-order refractive index differences. From the small difference in lipid droplet signal and the almost identical intensity profile in the CARS and NR-FWM images, we can conclude that the nonresonant background has significant contributions to the overall anti-Stokes signals at 2845 cm^{-1}. The vibrationally resonant contributions to the signal increase the intensity and contrast, but is not necessary for imaging the cellular morphology [see Figs. 3(d) and 3(e)]. It should be noted that, in general, the ratio between vibrationally resonant and NR-FWM signals depends on the Raman scattering cross-sections, feature sizes, and the electronic properties of the material. It is apparent that an excellent contrast can be obtained with NR-FWM imaging of cells, i.e., without the need to stimulate vibrationally resonant contributions contained in χ^3_R.

Figure 4(a) shows a combination of NR-FWM with TPEF and linear fluorescence. This figure shows that the fluorescence emission from cetuximab-IRdye 800CW (false color-coded as red) colocalizes with the cell membrane. Out-of-focus fluorescence emission, however, limits the axial resolution of the fluorescence image. The axial resolution of linear fluorescence is on the order of 2 μm, which is comparable to the average cell thickness. The lateral resolution of TPEF is on the order of 500 nm, which enables a better localization of the probe volume in the cell. The local minima in the Hoechst 33342 stained region colocalize with the nucleoli that are also clearly distinguishable in the NR-FWM image. Figure 4(b) shows an image obtained by subtracting the NR-FWM image at 2698 cm^{-1} from the CARS image at 2845 cm^{-1}. In this difference figure, the cell shape and lipid droplets can be identified. It can be seen here that the advantage of CARS imaging over NR-FWM imaging is mainly its suitability for molecule-specific imaging in this particular example.

Figure 5 shows a CARS [Fig. 5(a)] and NR-FWM [Fig. 5(b)] mixing image of a single A431 cell. The cellular morphology can be identified in both images. In the line profile plot in Fig 5(c), it can be seen that the lipid droplets generate more signal in the CARS image, as is also shown in Fig. 4(b).

For a quantitative comparison between the CARS and NR-FWM signals, the SNR is calculated for several regions in the cell shown in Figs. 3 and 5. The SNR is calculated according to Eq. (3).

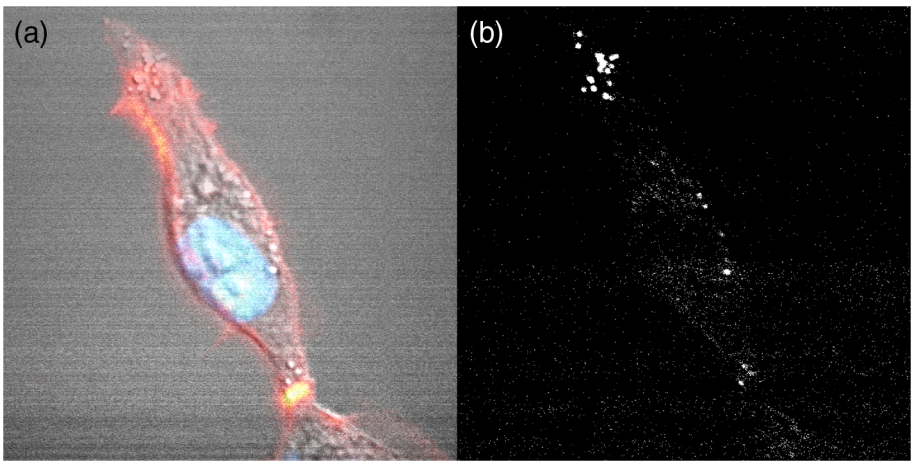

Fig. 4 (a) Overlay image of cetuximab-IRdye 800CW fluorescence emission, Hoechst 33342 TPEF fluorescence emission, and NR-FWM image at 2698 cm^{-1} (b) and difference figure NR-FWM at 2698 cm^{-1} subtracted from CARS image at 2845 cm^{-1}.

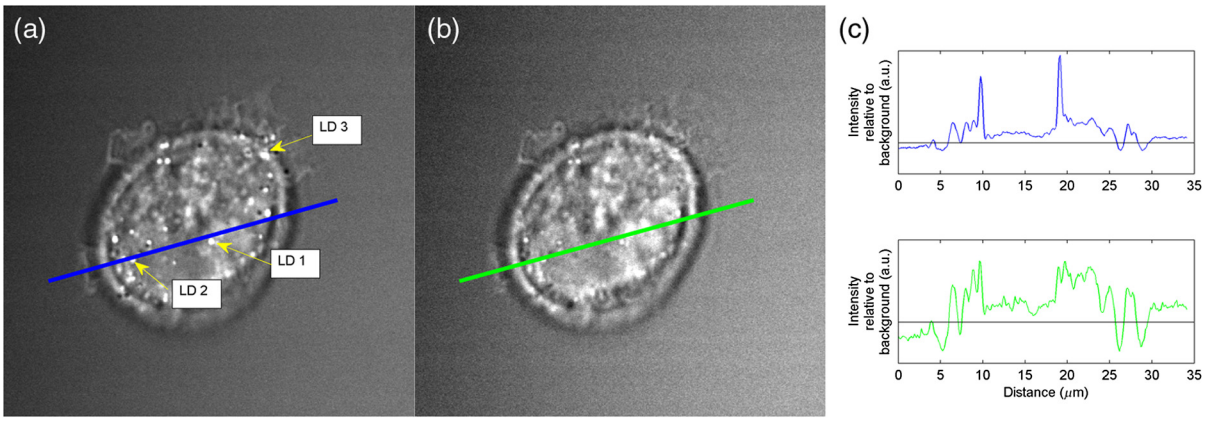

Fig. 5 (a) CARS and (b) NR-FWM image of a single A431 cell, recorded at 2845 and 2698 cm^{-1}, respectively. The field of view is 23×23 μm^2. (c) The line profile plots for the CARS and NR-FWM image are shown including the black line, indicating the average background intensity. Distance line starts at 0 μm at the left side of the image. The arrows in (a) indicate the LDs that were used for quantitative analysis in Table 2.

$$\text{SNR} = \frac{\text{Mean signal value}}{\text{Standard deviation background}}. \quad (3)$$

Table 1 shows the SNR for three lipid droplets indicated in Fig. 3 and for two different regions of the cell cytoplasm in both the CARS and NR-FWM images. Table 2 shows the SNR for three lipid droplets indicated in Fig. 5 and also for two different regions of the cell cytoplasm. In these two tables, it is shown that the SNR of the lipid droplets is approximately twice as large in the CARS image compared to the NR-FWM image. The SNR of the cell cytoplasm is only slightly larger in the CARS image compared to the NR-FWM image. Here the SNR in the CARS image increases only by an approximate factor 1.2 compared to the NR-FWM image.

The molecular properties of IRdye 800CW and the chosen excitation field frequencies cause photobleaching of IRdye 800CW while recording the TPEF, CARS, or NR-FWM images. This photodamage is a result of the relatively high excitation power required for the latter three modalities. Consequentially, first, the image of the linear fluorescence of IRdye 800CW was acquired and only then the nonlinear imaging modes were carried out.

Table 1 Signal-to-noise ratio calculated for several lipid droplets (shown in Fig. 3) and cytoplasm regions (not shown in Fig. 3).

	Signal-to-noise ratio in CARS image (mean ± standard deviation)	Signal-to-noise ratio in NR-FWM image (mean ± standard deviation)
Lipid droplet 1	19.89 ± 2.45	13.25 ± 2.30
Lipid droplet 2	28.20 ± 5.80	16.30 ± 2.28
Lipid droplet 3	14.74 ± 2.73	9.40 ± 2.20
Cell cytoplasm region 1	10.01 ± 1.43	8.00 ± 1.13
Cell cytoplasm region 2	15.73 ± 2.07	12.65 ± 1.62

Note: CARS, coherent anti-Stokes Raman scattering; NR-FWM, nonresonant four-wave mixing.

4.2 *Tumor Tissue Imaging*

Nonlinear imaging in combination with imaging of fluorescence-labeled cancer drugs was also applied to tumor tissue. Tumor tissue was imaged by collecting the single-photon excited fluorescence from pertuzumab-IRdye 800CW, TPEF of Hoechst, CARS at 2845 cm^{-1}, and NR-FWM at 2698 cm^{-1}. The tumor tissue was derived from an inoculated human breast cancer cell line SK-BR-3, which overexpresses HER2, xenografted in a mouse that was injected with the anti-HER2 antibody pertuzumab-IRdye 800CW.

Figure 6 shows the result of multimodal imaging of slices of tissue from the tumor xenograft, recorded at the same position in the sample. The distribution of pertuzumab-IRdye 800CW in the SK-BR-3 tumor is visualized in Fig. 6(a). Clearly, pertuzumab-IRdye 800CW is nonuniformly distributed in this tumor section and in individual cells. The location of the cell nuclei is subsequently visualized in the DAPI TPEF image in Fig. 6(b). The CARS image and the NR-FWM image in Figs. 6(c) and 6(d) show the morphology of the tumor tissue based on spatial

Table 2 Signal-to-noise ratio calculated for several lipid droplets (shown in Fig. 5) and cytoplasm regions (not shown in Fig. 5).

	Signal-to-noise ratio in CARS image (mean ± standard deviation)	Signal-to-noise ratio in NR-FWM image (mean ± standard deviation)
Lipid droplet 1	14.72 ± 4.14	6.48 ± 0.61
Lipid droplet 2	12.65 ± 3.05	6.40 ± 1.21
Lipid droplet 3	14.30 ± 3.87	6.58 ± 0.83
Cell cytoplasm region 1	5.67 ± 1.17	4.88 ± 0.85
Cell cytoplasm region 2	5.73 ± 0.91	5.11 ± 0.72

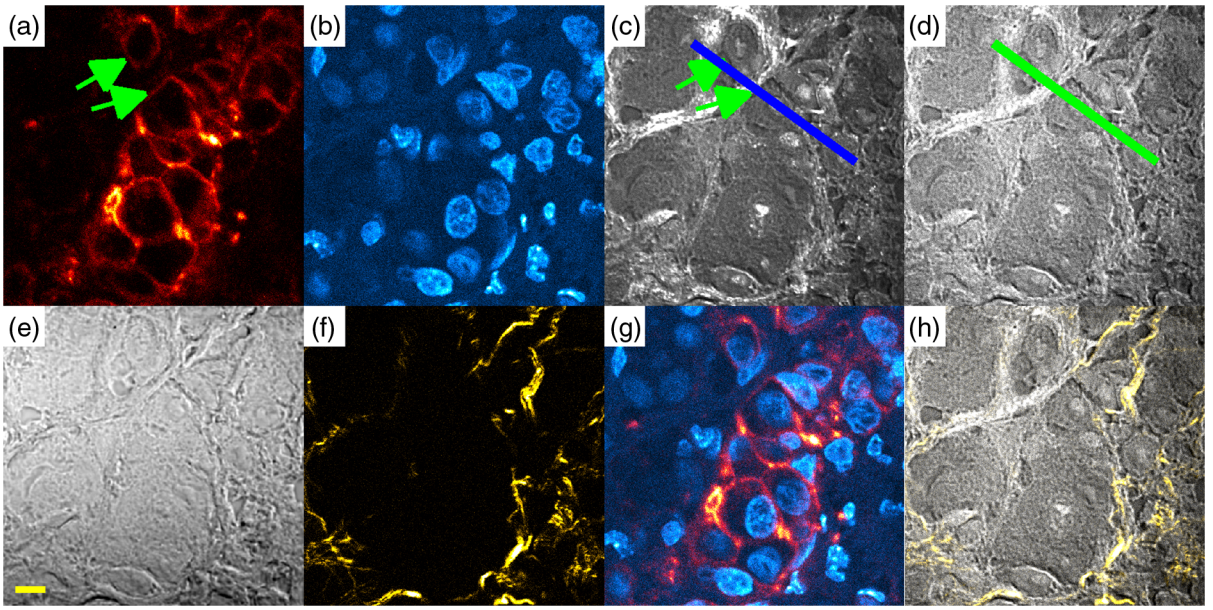

Fig. 6 Multimodal images of tumor slices obtained from a mouse bearing human breast cancer SK-BR-3 xenograft tumor, injected with pertuzumab-IRdye 800CW. The images show (a) distribution of pertuzumab-IRdye 800CW, (b) 4',6-diamidino-2-phenylindole (DAPI) stained cell nuclei, (c) tumor morphology using CARS at 2845 cm^{-1}, (d) tumor morphology using NR-FWM at 2698 cm^{-1}, (e) transmission image of tumor section, (f) collagen distribution using second harmonic generation (SHG), (g) overlay of pertuzumab and DAPI image, showing the distribution of pertuzumab with respect to the cell nuclei, and (h) overlay of collagen SHG and NR-FWM image. The size of the scale bar in (e) is 10 μm and is relevant for all panels from (a) to (h). The image size is 78×78 μm and consists of 1024×1024 pixels. The lines in (c) and (d) indicate the region used for the profile plot in Fig. 7.

variations in χ^3. In both these figures, cell nuclei can be identified. Also, in tissue sections, the nucleoli can be discriminated from surrounding nuclear components. Contrast between lipid-rich regions and tumor cells in the tumor section is clearly visible in both CARS and NR-FWM images. In the IRdye 800CW and DAPI overlay image in Fig. 6(g), the fluorescence emission shows the location of the cytoplasmic membrane of cells within the tumor. The fluorescence emission colocalizes with the boundary of some tumor cells that can be identified in the NR-FWM and CARS images (indicated with the green arrows in Fig. 6). This implies that the membrane has been stained, which is expected, because pertuzumab binds to receptor molecules on the cell membrane. Some nuclei can be identified in Fig. 6(g) that are not surrounded by an IRdye 800CW stained cytoplasmic membrane. These nuclei are smaller and differently shaped compared to the nuclei surrounded by an IRdye 800CW stained membrane. These cells could be native mouse cells present in the tumor. Also, the fact that the IRdye 800CW positive cells are grouped together and that the cells without a membrane stain are located outside of this region suggests that nonstained cells are native mouse cells. However, washing steps in the de-paraffinization step could also result in loss of fluorescent tracer from parts of the tumor tissue slice. Furthermore, lack of fluorescence could be due to necrosis in parts of the xenograft or represent residual pockets of Matrigel used in the xenografting of SK-BR-3 cells.

NR-FWM and CARS microscopy both provide significantly better contrast in this tumor sample than transmission microscopy, as can be seen from a comparison of the laser light transmission [Fig. 6(e)] with the NR-FWM and CARS images [Figs. 6(c) and 6(d)]. Especially due to the thickness (4 μm) of this tumor slice, NR-FWM and CARS are more suitable techniques for morphological imaging of this sample than transmission imaging. This is because the detected signal in CARS or NR-FWM is generated in a small confocal-like spot, whereas the transmission beam is affected by out-of-focus regions in the sample. Comparing the CARS and NR-FWM images and the corresponding line profile plots in Fig. 7, differences in relative intensities are observed. Both techniques provide label-free contrast in cellular and tissue imaging, where the vibrationally resonant part in the CARS images provides additional chemical

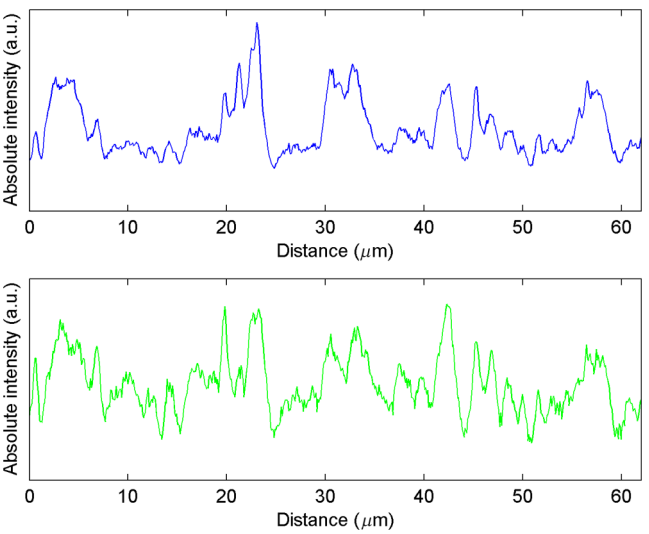

Fig. 7 Intensity profile plot of the blue (CARS image) and green (NR-FWM image) line in Fig. 6. Distance line starts at 0 μm at the left side of the image.

specific contrast. The distribution of collagen in the tumor is shown in Fig. 6(f), using SHG and overlaid with the NR-FWM image [Fig. 6(h)].

The suitability of NR-FWM imaging was demonstrated both in cells incubated with cetuximab-IRdye 800CW as well as in tumor xenograft tissue from animals injected with pertuzumab-IRdye800CW, respectively. Both cancer drugs show a membrane staining, as expected. In tumor tissue, where other components beside cells are also present, NR-FWM imaging is very suitable for morphological imaging.

5 Conclusion

We have demonstrated the potential of a multimodal microscopy combination of linear NIR fluorescence imaging with NR-FWM imaging to investigate the distribution of tumor-targeting drugs, such as cetuximab and pertuzumab, in cells and tissues. We have compared CARS imaging with NR-FWM imaging and have found that NR-FWM is an excellent approach to label-free cellular and tissue morphological imaging. The contrast in NR-FWM is based on spatial differences in χ^3, which is of a similar quality as vibrationally resonant CARS. It can be concluded that the vibrationally resonant contribution to the total anti-Stokes signal is not essential to provide high-contrast images based on general total χ^3.

From comparing CARS and NR-FWM quantitatively, it can be concluded that small lipid droplets inside cells provide approximately a twofold SNR compared to NR-FWM. The contrast in regions of the cell that contain mostly cytoplasm and without clearly visible organelles shows minor differences between CARS and NR-FWM images.

By creating a hybrid microscope system that integrates linear fluorescence, TPEF, SHG, laser light transmission imaging and coherent anti-Stokes Raman scattering, and NR-FWM, it is possible to selectively image fluorescently labeled cancer drugs and obtain morphology information about target location of the drugs in the cell or tumor tissue.

For future work, a combination of NR-FWM with confocal linear fluorescence will provide a better resolution for fluorescence imaging and could be used for numerous applications in biological imaging, including resolving the subcellular distribution of fluorescently labeled drugs in axial and lateral direction.

Acknowledgments

We thank Erik Garbacik and Aufried Lenferink (UT, the Netherlands) for technical support and Bente Elschot (UT) for her input and discussions. We are thankful to APE Berlin for providing the optical parametric oscillator and to Coherent Inc. for the Paladin laser. This work is conducted as part of the OnQview ERC Advanced grant (ERC-2011-ADG, ID1).

References

1. W. Wang, E. Q. Wang, and J. P. Balthasar, "Monoclonal antibody pharmacokinetics and pharmacodynamics," *Clin. Pharmacol. Ther.* **84**(5), 548–558 (2008).
2. Y. Yarden, "Biology of HER2 and its importance in breast cancer," *Oncology* **61**(2), 1–13 (2001).
3. Y. Yarden and M. X. Sliwkowski, "Untangling the ErbB signalling network," *Nat. Rev.* **2**(2), 127–137 (2001).
4. A. G. T. Terwisscha van Scheltinga et al., "Intraoperative near-infrared fluorescence tumor imaging with vascular endothelial growth factor and human epidermal growth factor receptor 2 targeting antibodies," *J. Nucl. Med.* **52**(11), 1778–1785 (2011).
5. A. A. Heikal, "Intracellular coenzymes as natural biomarkers for metabolic activities and mitochondrial anomalies," *Biomark. Med.* **4**(2), 241–263 (2010).
6. R. R. Anderson and J. A. Parrish, "The optics of human skin," *J. Invest. Dermatol.* **77**, 13–19 (1981).
7. M. V. Marshall et al., "Single-dose intravenous toxicity study of IRdye 800CW in Sprague-Dawley rats," *Mol. Imaging. Biol.* **12**(6), 583–594 (2010).
8. A. E. Foster et al., "In vivo fluorescent optical imaging of cytotoxic T lymphocyte migration using IRDye 800CW near-infrared dye," *Appl. Opt.* **47**(31), 5944–5952 (2008).
9. J. H. E. Baker et al., "Direct visualization of heterogeneous extravascular distribution of trastuzumab in human epidermal growth factor receptor type 2 overexpressing xenografts," *Clin. Cancer Res.* **14**(7), 2171–2179 (2008).
10. C. M. Lee and I. F. Tannock, "The distribution of the therapeutic monoclonal antibodies cetuximab and trastuzumab within solid tumors," *BMC Cancer* **10**, 255 (2010).
11. J. H. Ryu et al., "In vivo fluorescence imaging for cancer diagnosis using receptor-targeted epidermal growth factor-based nanoprobe," *Biomaterials* **34**, 9149–9159 (2013).
12. Y. Zhao et al., "Longitudinal label-free tracking of cell death dynamics in living engineered human skin tissue with a multimodal microscope," *Biomed. Opt. Express* **5**(10), 3699–3716 (2014).
13. C. L. Evans and X. S. Xie, "Coherent anti-Stokes Raman scattering microscopy: chemical imaging for biology and medicine," *Ann. Rev. Anal. Chem.* **1**(1), 883–909 (2008).
14. C. J. Strachan, M. Windbergs, and H. L. Offerhaus, "Pharmaceutical applications of non-linear imaging," *Int. J. Pharm.* **417**(1–2), 163–172 (2011).
15. R. Mouras et al., "Nonlinear optical microscopy for drug delivery monitoring and cancer tissue imaging," *J. Raman Spectrosc.* **41**(8), 848–852 (2010).
16. R. Mouras et al., "Multimodal, label-free nonlinear optical imaging for applications in biology and biomedical science," *J. Raman Spectrosc.* **44**(10), 1373–1378 (2013).
17. E. O. Potma, C. L. Evans, and X. S. Xie, "Heterodyne coherent anti-Stokes Raman scattering (CARS) imaging," *Opt. Lett.* **31**(2), 241–243 (2006).
18. F. Masia et al., "Resonant four-wave mixing of gold nanoparticles for three-dimensional cell microscopy," *Opt. Lett.* **34**(12), 1816–1818 (2009).
19. S. A. Akhmanov et al., "Coherent ellipsometry of Raman scattering of light," *JETP Lett.* **25**, 416–420 (1977).
20. J. X. Cheng, L. D. Book, and X. S. Xie, "Polarization coherent anti-Stokes Raman scattering microscopy," *Opt. Lett.* **26**(17), 1341–1343 (2001).
21. F. Ganikhanov et al., "High-sensitivity vibrational imaging with frequency modulation coherent anti-Stokes Raman scattering (FM CARS) microscopy," *Opt Lett.* **31**(12), 1872–1874 (2006).
22. P. Mahou et al., "Combined third-harmonic generation and four-wave mixing microscopy of tissues and embryos," *Biomed. Opt. Express* **2**(10), 2837–2849 (2011).
23. W. Min et al., "Near-degenerate four-wave mixing microscopy," *Nano Lett.* **1**(1), 1–4 (2009).
24. T. W. Tukker, C. Otto, and J. Greve, "Design, optimization, and characterization of a narrow-bandwidth optical parametric oscillator," *J. Opt. Soc. Am. B* **16**(1), 90–95 (1999).
25. H. Yamakoshi et al., "Imaging of EdU, an alkyne-tagged cell proliferation probe, by Raman microscopy," *J. Am. Chem. Soc.* **133**(16), 6102–6105 (2011).
26. H. J. van Manen, A. Lenferink, and C. Otto, "Noninvasive imaging of protein metabolic labeling in single human cells using stable isotopes and Raman microscopy," *Anal. Chem.* **80**(24), 9576–9582 (2008).
27. T. T. Le, S. Yue, and J.-X. Cheng, "Shedding new light on lipid biology with coherent anti-Stokes Raman scattering microscopy," *J. Lipid Res.* **51**(11), 3091–3102 (2010).

Biographies for the authors are not available.